



HAL
open science

Polarization structure of nanostrip domain intersections in GeTe films

Boris Croes, Fabien Cheynis, Salia Cherifi Cherifi-Hertel, Kokou Dodzi
Dorkenoo, Pierre Müller, Stefano Curiotto, Frédéric Leroy

► **To cite this version:**

Boris Croes, Fabien Cheynis, Salia Cherifi Cherifi-Hertel, Kokou Dodzi Dorkenoo, Pierre Müller, et al.. Polarization structure of nanostrip domain intersections in GeTe films. *Physical Review B*, 2024, 109 (2), pp.024103. 10.1103/PhysRevB.109.024103 . hal-04403228

HAL Id: hal-04403228

<https://hal.science/hal-04403228>

Submitted on 18 Jan 2024

HAL is a multi-disciplinary open access archive for the deposit and dissemination of scientific research documents, whether they are published or not. The documents may come from teaching and research institutions in France or abroad, or from public or private research centers.

L'archive ouverte pluridisciplinaire **HAL**, est destinée au dépôt et à la diffusion de documents scientifiques de niveau recherche, publiés ou non, émanant des établissements d'enseignement et de recherche français ou étrangers, des laboratoires publics ou privés.

Polarization structure of nanostrip domain intersections in GeTe films

Boris Croes,^{1,2} Fabien Cheynis,¹ Salia Cherifi-Hertel,² Kokou Dodzi Dorkenoo,² Pierre Müller,¹ Stefano Curiotto,¹ and Frédéric Leroy¹

¹*Aix Marseille Univ, CNRS, CINAM, AMU-TECH, Marseille, France*

²*Université de Strasbourg, CNRS, Institut de Physique et Chimie des Matériaux de Strasbourg, Strasbourg, 67000, France*

(Dated: December 7, 2023)

Ferroelectric germanium telluride is under active consideration for spintronic and thermoelectric applications. The control of the ferroelectric domain walls is a key issue to optimize the electronic and thermal properties of GeTe thin films. Domain walls properties are usually driven by the mechanical and electrostatic compatibility conditions of twin domains. However in dense ferroelectric domain structures these compatibility conditions are hardly fulfilled everywhere. In particular intersection of domains may result in complex lattice relaxations and polarization textures. In this study, we have fabricated GeTe thin films on silicon substrate and elucidated the intersections of a -type domains using 3D reciprocal space maps, scanning tunneling microscopy and second-harmonic microscopy. We demonstrate the presence of complex structural reorganizations, that manifest by the formation of charged domain walls, large lattice rotations and enhanced stretching of the rhombohedral lattice.

I. INTRODUCTION

Ferroelectric thin films are the object of intense fundamental research stimulated by their applications as functional materials. The ability to synthesize ferroelectric thin films of high crystalline quality based on layer-by-layer growth techniques and strain engineering has made possible to discover novel phenomena based on the interplay between the stress induced by the substrate and the electrostatic boundary conditions. It has been demonstrated that flux-closure polar domains [1–3], vortices [4 and 5] and even skyrmions [6] could be obtained in ferroelectric materials. These novel structures can potentially exhibit enhanced electric conduction as measured at vortex cores in BiFeO₃ [2], high thermal resistance [7], or high Seebeck coefficient at charged domain walls [8]. Such properties could be used in future devices if the local ferroelectric polarization can be controlled. In the quest of enhanced ferroelectric properties, intersections of domain walls are expected to show highly polarized regions with complex polarization textures resulting from a strong relaxation of the lattice. Among ferroelectrics, GeTe has witnessed a sustained boom [9–14]. As a thermoelectrics, it has recently been demonstrated a record figure of merit ($zT \sim 2.4$) at 330°C for the ferroelectric GeTe phase [15]. In the meantime, major results have been obtained on ferroelectric GeTe thin films in the context of spintronic properties based on the Rashba effect [16]. It has been demonstrated the reversal of the ferroelectric polarization under an electric field [17] and a consistent change of the spin chirality of the band structure [18 and 19]. Even more fascinating GeTe thin films show remarkable transport properties at room temperature such as non-reciprocal charge transport [20] or ferroelectric switching of the spin-to-charge conversion [21].

All these results take advantage of the ferroelectric property of α -GeTe. This phase has a rhombohedral structure (space group R3m) and bulk Curie temperature well above room temperature ($T_c \sim 650 - 700$ K). The

spontaneous polarization of α -GeTe is along the pseudocubic $\langle 111 \rangle_c$ leading to the formation of 4 ferroelastic variants (c stands for pseudo-cubic coordinates, see supplementary materials [22]). As reported by Wang et al. [23] α -GeTe thin films can be grown with a quasi-single crystalline quality on Si(111) by molecular beam epitaxy using a pre-deposition of 1 monolayer of Sb onto the substrate. Despite a significant lattice mismatch of $\sim 8.5\%$ with the substrate, the GeTe layer is relaxed since the very beginning of growth. Croes et al. [24] have shown that GeTe thin films thicker than 30 nm have a multiple domain structure with all 4 ferroelastic variants. The main domain has a ferroelectric polarization perpendicular to the surface, *i.e.* in the $[111]_c$ direction, and is called c -domain. The three other ferroelectric domains are called hereafter a -domains and form 71° -type domain walls with the c -domain. These domain walls ensure mechanical compatibility and neutrality of the interface between a - and c -domains. In addition to the a/c twin domains, the simultaneous existence of different variants of a -domains generates inevitably a/a 109° -type intersections.

In this article we address the intersection of a -domains in GeTe thin films and explore the formation of non-trivial polarization configurations. Since a -domains are already constrained by the interaction with the majority c -domain that is in epitaxy with the Si substrate, the crossing of a -domains generates major problems of mechanical and electrical compatibilities. We show that a huge structural lattice reorganization occurs and new domain walls are formed. In particular the rhombohedral lattice angle decreases by 1° , the lattice rotates by more than 4° and a periodic network of charged domain walls is formed perpendicular to the surface plane. These results, addressed by 3D reciprocal space maps and scanning tunneling microscopy, point to a complex polarization texture of GeTe thin films at a/a intersections while second-harmonic generation (SHG), supported by machine learning methods, reveals different crossing types and an unchanged symmetry at the intersection regions.

II. EXPERIMENTAL METHOD

Si(111) wafers (Siltronix; 550 μm -thick; $\rho=1\text{-}10\ \Omega\text{cm}$) are first cleaned by acetone and ethanol rinsing before introduction in ultra-high vacuum (UHV, 10^{-8} Pa). Then the substrates are degassed at 1000 K during 12 h followed by repeated high temperature annealing (1500 K) during a few minutes in order to obtain a clean 7×7 surface reconstruction. First a deposition of 1 monolayer of Sb is performed on the Si(111) surface, forming the so-called Si(111)- $\sqrt{3}\times\sqrt{3}$ -Sb reconstruction that greatly improves the crystalline quality of the GeTe film [23]. The GeTe thin films are grown by co-deposition of Ge (1175 $^{\circ}\text{C}$) and Te (310 $^{\circ}\text{C}$) in UHV on a sample maintained at 275 $^{\circ}\text{C}$. In these conditions the flux ratio between Ge:Te is fixed at 2:5 in order to compensate for the high desorption rate of Te [25]. All the deposition sources are effusion cells from MBE-Komponenten GmbH. After growth, the samples are transferred under UHV conditions thanks to a homemade transfer suitcase and characterized by scanning tunneling microscopy (STM) with a VT-STM (Scienta Omicron GmbH). STM images were obtained at room temperature in constant current mode with typical imaging conditions (U=-1 V, I= 20 pA, W tip). The internal structure of thick GeTe films (>40 nm) has been studied by x-ray diffraction at BM32 beamline (ESRF). X-ray diffraction data have been measured at 18 keV [$\lambda=0.06888$ nm] with a beam size of $200\times 300\ \mu\text{m}^2$ and collected onto a 2D detector. The data have been converted from the detector coordinates (pixel index) to diffraction angles and then to reciprocal space coordinates. To protect the GeTe surface from contamination during sample transfer to the ESRF UHV chamber, a Te capping was used. The capping is removed in UHV first by a mild Ar ion bombardment at room temperature (1 keV, 10 μA) to remove the top most oxidized layers then by annealing at 220 $^{\circ}\text{C}$ to desorb the complete Te layer. Second-harmonic generation (SHG) microscopy and polarimetry measurements are conducted in an inverted optical microscope. The fundamental wave is provided by a laser source emitting pulses of 100 fs duration at a repetition rate of 80 MHz, centered at a wavelength $\lambda = 800$ nm. The sample is illuminated at normal incidence with a time-averaged power of about 10 mW. The SHG images are obtained by scanning the sample with respect to the focused laser beam (objective $\times 60$, 0.85 numerical aperture) using computer-controlled stepping motors. The output intensity is spectrally filtered and collected into a photomultiplier. Polarimetry measurements are performed by recording the SHG images at different polarizer and analyzer angles (ϕ and α , respectively) [26]. The automatic polarimetry data analysis is supported by machine learning methods [27] for fast and efficient detection of the nanostrip domain crossing regions. The analysis workflow presented in this study is implemented using Python 3. The program allows us to load and preprocess the SHG data cube (stack of images recorded at different polarizer and analyzer configurations) and

display the results. The K-means and Non-negative Matrix Factorization (NMF) algorithms are implemented via open-access Python packages [28] and applied to the SHG polarimetry data for the automatic determination of the domain variants as detailed in Ref. [27].

III. RESULTS AND DISCUSSION

The surface morphology of a 800 nm-thick GeTe film grown on Si(111)- $\sqrt{3}\times\sqrt{3}$ -Sb surface shows needle shape structures [figure 1(a)] crossing the surface over several microns in the $\langle 1\bar{1}0 \rangle_c$ directions. These needles are a few hundreds of nanometer wide and show a slightly tilted surface plane with respect to the main surface. These needles point out the presence of ferroelectric a -domains whereas the flat layer is made of the c -domain [24]. The corresponding 3D reciprocal space map around the symmetric Bragg peak of GeTe, perpendicular to the surface plane, shows indeed four contributions [see figure 1(d)]. The main one labeled 222_c , at low q_z , is due to the majority c -domain with a rhombohedron axis of the unit cell normal to the surface. The three other Bragg peaks $2\bar{2}2_c$, $2\bar{2}2_c$ and $2\bar{2}2_c$ at higher q_z and slightly off the specular rod by 1.4° , are due to three a -domains variants with axes of the rhombohedron unit cell tilted by $\sim 71^{\circ}$ with respect to the normal to the surface. As can be seen on figure 1(a), the density of a -domains in thick GeTe films is such that crossing of a -domains frequently occurs. Figure 1(b) shows a close view of the GeTe surface by STM. The derivative of the surface morphology highlights specific surface structures [figure 1(c)]. The thinnest dark lines correspond to atomic steps. The a -domains appear as needles with a grey contrast due to the tilt angle of the surface plane. Their typical width is 100-200 nm. In this region all three variants of a -domains exist and when two a -domains intersect they form a staircase surface morphology with a typical period of 30–50 nm along the $\langle 1\bar{1}0 \rangle_c$ direction [see figures 1(b)-(c)]. The morphology of the intersection is translation-invariant along the $\langle 11\bar{2} \rangle_c$ direction, i.e. along the bisector of the intersecting a -domains. This local change of surface morphology claims for a change of domain walls.

To address these changes we have characterized the surface topography by STM in combination with 3D reciprocal space map analysis. The height profile of the intersecting area along the translation-invariant $[\bar{2}11]_c$ direction shows a small angle of $0.8^{\circ}\pm 0.1^{\circ}$ of the surface plane with respect to the flat c -domain [figure 2(b)]. This angle corresponds to the angle of the intersecting line of two tilted surface planes of two a -domains with respect to the c -domain surface ($1.4^{\circ}\times\cos(60^{\circ}) = 0.7^{\circ}$). In reciprocal space such a tilted surface should give a contribution in-between the Bragg peaks of two a -domains. Indeed by reducing the iso-intensity surface of the 3D reciprocal space map around a -domain Bragg peaks, we observe some diffuse scattering at this reciprocal space coordinate [figure 2(e)]. Even more, the 3D reciprocal space

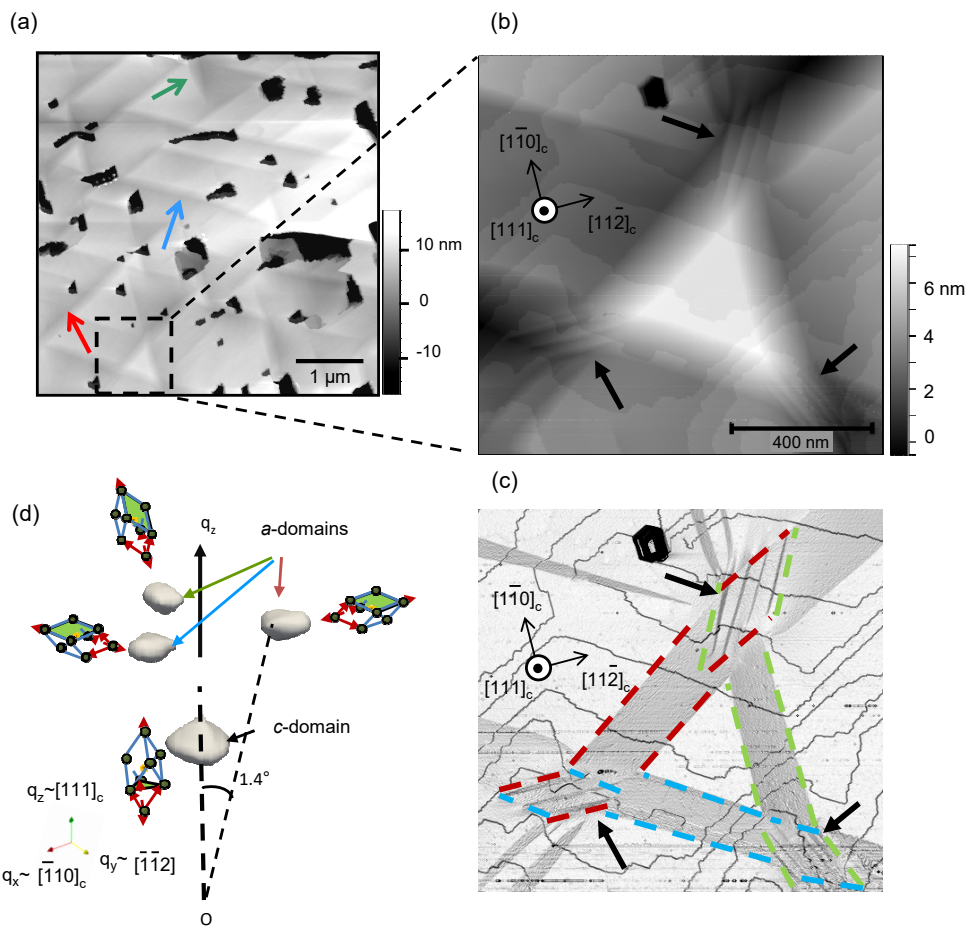


FIG. 1. (a) STM image of a 800 nm-thick GeTe thin film grown on Si(111)- $\sqrt{3} \times \sqrt{3}$ -Sb ($U=-1$ V, $I=20$ pA). The arrows show needle-shape a -type domains at the surface. The colors indicates the three variants of a -domains. (b) Close view of three domains crossing showing the staircase morphology (black arrows). (c) Derivative of STM image (b) to highlight the morphological slopes at the surface corresponding to a -domains surface and a/a crossings. (d) 3D reciprocal space map of 222_c , $2\bar{2}\bar{2}_c$ $2\bar{2}\bar{2}_c$ and $\bar{2}\bar{2}\bar{2}_c$ GeTe Bragg peaks. q_x , q_y and q_z are the reciprocal space coordinates that are aligned respectively along $[\bar{1}10]_c$, $[\bar{1}12]_c$ and $[111]_c$ directions. The main peak at $(0, 0, 35.40 \text{ nm}^{-1})$ coordinate arises from the major c -domain (rhombohedron axis perpendicular to surface) and the three other Bragg peaks, at higher q_z $[(0, -0.96, 36.73 \text{ nm}^{-1})$, $(-0.80, 0.46, 36.72 \text{ nm}^{-1})$ and $(0.70, 0.50, 36.71 \text{ nm}^{-1})$], result from the three a -domains with rhombohedron axis nearly in-plane. The surface planes of the a -domains are tilted by 1.4° with respect to the Si(111) surface.

197 map shows an arc of diffuse scattering that connects each
 198 Bragg peak of a -domains. This signal suggests a strong
 199 interaction between intersecting a -domains that can be
 200 assigned to a lattice relaxation process. In particular the
 201 diffuse scattering arc suggests not only a mean lattice ro-
 202 tation towards the $\langle \bar{1}\bar{1}2 \rangle_c$ direction by $\beta=0.8^\circ$ but also
 203 towards the $\langle \bar{1}10 \rangle_c$ direction [angle α , see figures 2(d)-
 204 (e)]. Indeed the STM height profile of the staircase mor-
 205 phology shows large slope variations of the surface that
 206 should give x-ray diffuse scattering contributions along
 207 the connecting arc [figure 2(c)]. Let us note that the
 208 x-ray diffraction measurement provides a continuous arc
 209 since it is based on a macroscopic sampling of the lattice
 210 relaxations at domain intersections whereas STM images
 211 provide a local characterization with a few measured tilt
 212 angles corresponding to a local relaxation state. To be

213 complete, let us not that figure 2(e) shows also diffuse
 214 scattering rods connecting a - and c -domains Bragg peaks.
 215 As shown by Croes et al. [24] this diffuse scattering origi-
 216 nates from the faceted interface associated with a/c do-
 217 main walls (71° -type domain wall). The domain walls
 218 generate diffuse scattering rods, called crystal truncation
 219 rods for surfaces, starting on each Bragg peaks of the
 220 corresponding a - and c -domains and extending perpen-
 221 dicular to the domain wall, forming the measured diffuse
 222 scattering tails.

223 The vertical cross-section of the 3D reciprocal space
 224 map passing through two Bragg peaks of a -type domains
 225 using a lower iso-intensity value brings additional infor-
 226 mation on the crossings [see figure 3(a)]. It shows that
 227 the diffuse scattering arc is not simply connecting the two
 228 Bragg reflections. It is in fact composed of two diffuse

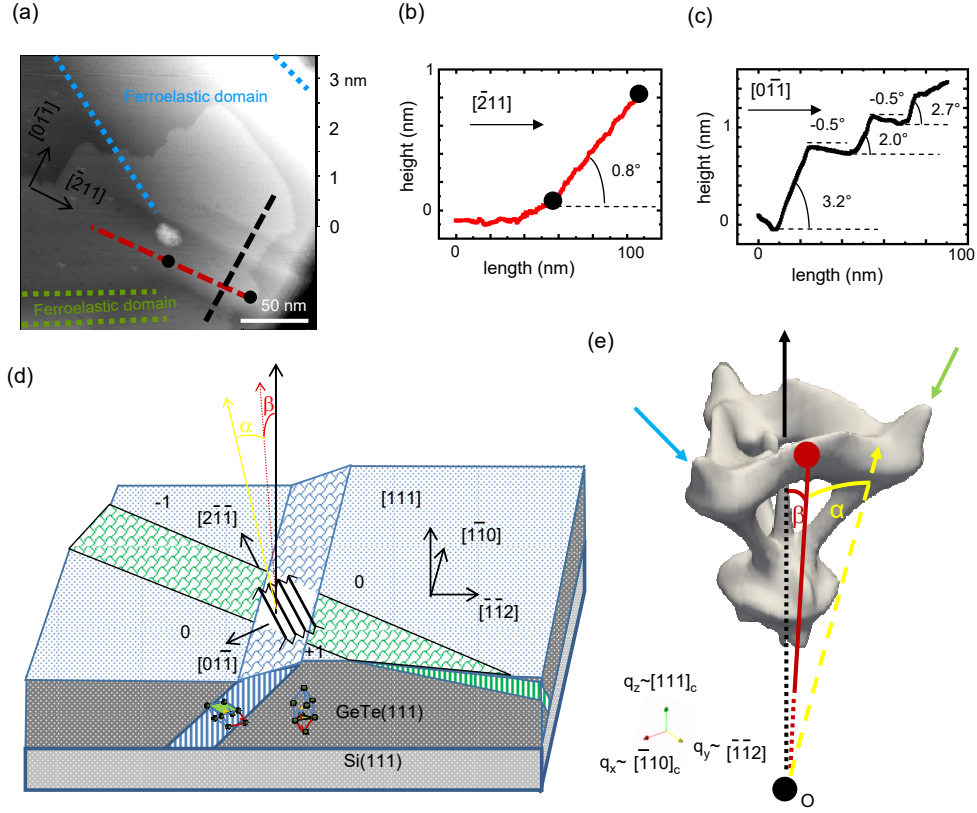


FIG. 2. (a) STM image of an intersection area of two a -domains. (b) Line profile along the $[\bar{2}11]_c$ direction [along red dashed line in (a)] showing a slight tilt angle of the edge. (c) Line profile along the $[0\bar{1}1]_c$ direction [along dark dashed line in (a)] showing a staircase morphology of the surface. (d) Schematic view of the GeTe film, c - and a -type ferroelastic domains as well as a a/a intersection. The rhombohedron unit cell is given in the c -domain and in a a -domain. The two a -domains extend as stripes elongated along $[10\bar{1}]_c$ and $[\bar{1}\bar{1}0]_c$ directions. Their crossing forms a staircase morphology (black lines) along $[0\bar{1}1]_c$ that is translation invariant along $[\bar{2}11]_c$ direction. α represents the tilt angle of the surface with respect to $[111]_c$ and oriented in $[0\bar{1}1]_c$ direction. β represents the tilt angle of the surface with respect to $[111]_c$ and oriented in $[\bar{2}11]_c$ direction. (e) 3D reciprocal space maps around 222_c , $2\bar{2}\bar{2}_c$, $22\bar{2}_c$ and $\bar{2}\bar{2}2_c$ GeTe Bragg peaks: the x-ray scattered intensity arising from the intersections is expected to be in-between 2 Bragg peaks. The corresponding diffuse scattering is tilted by an angle β with respect to the c -axis in the $[\bar{1}\bar{1}2]_c$ direction and the staircase morphology generates a diffuse arc tilted by an angle α in the $[\bar{1}\bar{1}0]_c$ direction.

229 tails that start at each Bragg peak and extend towards
 230 the neighboring Bragg peak, passing slightly above and
 231 continuing even further away forming an arc of a circle (green and blue dashed lines). This surprising result
 232 shows that huge rotations of the GeTe lattice occur in
 233 the intersection zone. As the diffuse tail from one Bragg
 234 peak extends to the neighboring Bragg peak (and vice-
 235 versa), then we can say that the surface planes of two
 236 intersecting a -domains rotate so much that they appear
 237 to exchange their surface tilt angles in the crossing area.
 238 As this diffuse scattering is measured even further away
 239 from the neighboring Bragg peak, this indicates that the
 240 surface angle of one a -domain can be more tilted than the
 241 neighboring a -domain (away from the intersection area).
 242 This x-ray diffraction result is corroborated by high res-
 243 olution STM images. A close view of the intersecting
 244 area of two a -domains shows the details of the surface
 245 structure [figure 3(b)]. As shown by Croes and coworkers
 246 [29], the surface termination of a -domains displays sur-
 247 face reconstructions with large unit cells designed as row
 248 and scale structures. One can observe in the intersection
 249 area that the slope change of the staircase morphology
 250 is associated with a change of orientation of the surface
 251 reconstruction. If we associate the surface reconstruction
 252 with each a -domain we observe that the surface normal of
 253 a a -domain alone (without intersection) is tilted by $\alpha =$
 254 -1.1° in the $[0\bar{1}1]_c$ direction as expected from mechanical
 255 compatibility with the c -domain [$-1.2^\circ = -1.4^\circ \times \cos(30^\circ)$]
 256 whereas it is tilted by $\alpha = +3.2^\circ$, $+2.0^\circ$ and $+2.7^\circ$ in the
 257 a/a intersection area. Similarly the other a -domain is
 258 tilted by $\alpha = +1.1^\circ$ in the $[0\bar{1}1]_c$ direction as expected
 259 from mechanical compatibility with the c -domain but
 260 tilted by -0.5° in the intersection area. In figure 3(c) are
 261 schematically shown the expected positions of the x-ray
 262

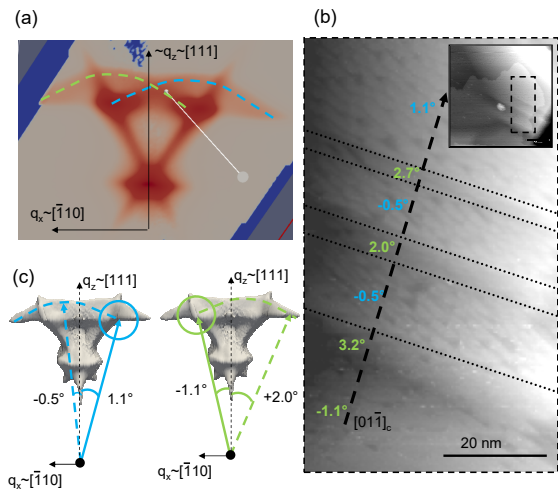


FIG. 3. (a) Cross-section of the 3D reciprocal space map passing through the Bragg peaks of two a -domains. Evidence of two crossing diffuse tails are highlighted by dashed lines. (b) Close STM view of the surface reconstruction of intersecting domains (inset: large view of the surface and corresponding imaged area). The dashed lines separate the areas with specific surface reconstructions and thus identify different a -domain type. The indicated surface angles along $[01\bar{1}]_c$ direction are indicated in blue or green depending on the a -domain [values extracted from the height profile of figure 2(c)]. (c) 3D reciprocal space maps and schematic representation of the corresponding expected x-ray scattered intensity from typical measured surface tilt angles by STM.

263 scattering signal on the 3D-reciprocal space map assum-
 264 ing similar lattice rotations. They perfectly fit on the
 265 diffuse scattering arc.

266 To interpret this result let us study the mechanical
 267 compatibility conditions of two intersecting a -domains.
 268 At first, i.e. away from a/a intersection, both a -domains
 269 form 71° -type domain walls with the majority c -domain
 270 [24]. Assuming that the c -domain keeps a planar in-
 271 terface with the Si(111) substrate then the $(111)_c$
 272 surface planes of a -domains are expected to be tilted by
 273 1.39° as deduced from the rhombohedral angle (58.3°)
 274 of GeTe and mechanical compatibility conditions at 71° -
 275 type domain walls. This is indeed confirmed by STM
 276 observations and x-ray diffraction ($\sim 1.4^\circ$). The theo-
 277 retical 1.39° tilt angle [24] can be decomposed in a ro-
 278 tation of the lattice (2.08°) and a pure shear compo-
 279 nent (-0.69°). This geometrical result is schematically
 280 illustrated in figures 4-(a)-(b) showing the tilt angles of
 281 $(111)_c$ surface planes of two a -domains with rhombohe-
 282 dron axes along $[11\bar{1}]_c$ and $[\bar{1}11]_c$ (the coordinates refer
 283 to the c -domains pseudo-cube). However in the intersec-
 284 tion area, a staircase morphology is observed. This indi-
 285 cates a local rearrangement of polarization and the exist-
 286 ence of additional domain patterns separated by domain
 287 walls. From the symmetry properties of rhombohedral
 288 GeTe and translation-invariance of the staircase morphol-
 289 ogy along $\langle 11\bar{2} \rangle_c$ we can estimate that a/a domain walls

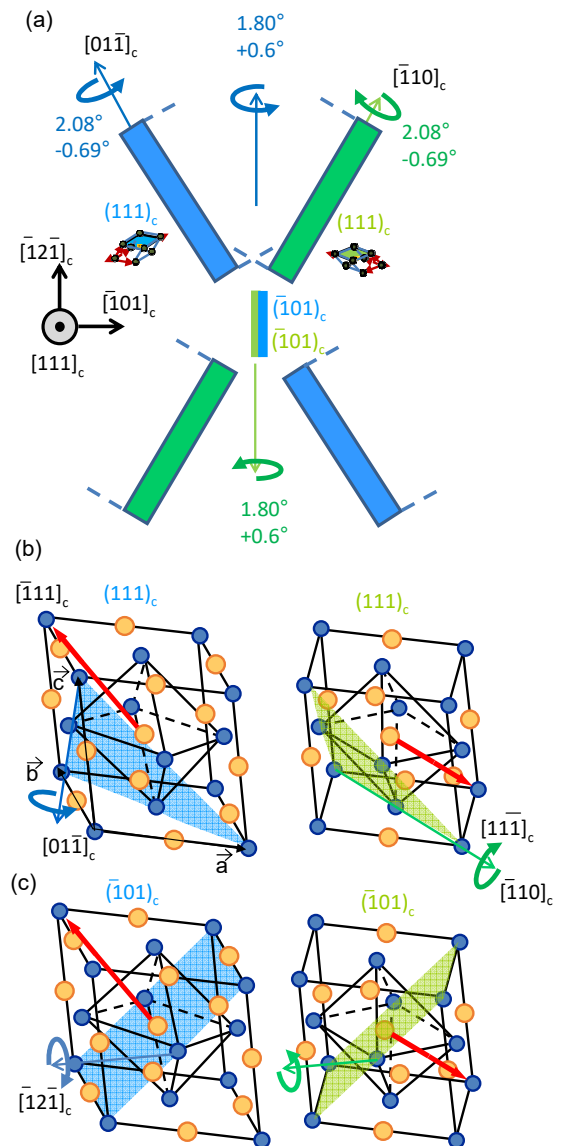


FIG. 4. (a) Schematic representation of two intersecting a -domains. Considering pseudo-cubic unit cells, the $(111)_c$ surface planes and the $(\bar{1}01)_c$ domain wall planes are represented with their rotations (without intersection). The $(111)_c$ surface plane of a -domains is expected to be tilted by $2.08^\circ - 0.69^\circ = 1.39^\circ$ with respect to Si(111) surface (2.08° from lattice rotation and -0.69° from shear). The $(\bar{1}01)_c$ domain wall plane of a -domains is expected to be tilted by $1.80^\circ + 0.60^\circ = 2.40^\circ$ with respect to Si($\bar{1}01$) $_c$ plane (1.80° from lattice rotation and $+0.60^\circ$ from shear). (b) Same as (a) but representing the pseudo-cubic unit cells for two a -domains elongated along $[\bar{1}11]_c$ and $[11\bar{1}]_c$. The filled areas (blue and green) represent the $(111)_c$ surface plane that tilts due to the stretching of the rhombohedron. (c) Same as (b) but considering the tilt of the $(\bar{1}01)_c$ plane corresponding to the domain wall generated by the a/a intersection.

are $(\bar{1}01)_c$ crystallographic planes forming 109° -type domain wall that are perpendicular to the $(111)_c$ surface plane. Such domain walls necessitate a reorganization of the crystal lattice to minimize the interfacial strain field at a/a crossing. In particular one can quantify the necessary rotation to ensure mechanical compatibility at such an interface. Figure 4-(c) shows a schematic representation of the tilt angles of $(\bar{1}01)_c$ crystallographic plane of two a -domains with rhombohedron axes along $[11\bar{1}]_c$ and $[\bar{1}11]_c$. In absence of intersection, the $(\bar{1}01)_c$ crystallographic planes of two a -domains are tilted with respect to the $[\bar{1}2\bar{1}]_c$ axis in opposed directions by $+2.4^\circ$ and -2.4° [1.8° arises from the rotation imposed by the a/c mechanical compatibility and $+0.60^\circ$ from pure shear, see figure 4-(a)]. To force the two crystal lattices to mechanically match in the same $(\bar{1}01)_c$ plane, a rotation of the crystals towards each other by $2.4 \times 2 = 4.8^\circ$ is necessary. In this circumstance either both domains rotate simultaneously or alternatively. STM image of figure 3(b) shows that both domains rotate alternatively and form a staircase surface morphology. The smallest domain (width) at the intersection undergoes the largest rotation. For instance, outside the intersection area, the surface plane of the smallest a -domain in figure 3(b) is tilted by $\alpha = -1.1^\circ$ and in the intersecting area, it can rotate around the $[\bar{1}2\bar{1}]_c$ axis by $+4.3^\circ$ to reach $\alpha = +3.2^\circ$ at maximum. The largest a -domain rotates less (-1.6°), from $\alpha = +1.1^\circ$ outside the intersecting area to $\alpha = -0.5^\circ$ inside. From these measurements we observe that the rotations of the a -domains in the intersection areas are extremely large but not enough to achieve a complete lattice relaxation at the domain wall (4.8°). This points to a residual stress due to the additional mechanical contributions related to the interface with the c -domains and to the epitaxy with the Si substrate. In addition let us note that the observed rotation of the lattices to adjust the $(\bar{1}01)_c$ domain wall of two intersecting a -domains should not occur only around the $[\bar{1}2\bar{1}]_c$ axis. The $(\bar{1}01)_c$ plane is also expected to rotate by 0.85° around the surface normal in opposed directions for both a -domains to be mechanically compatible. This rotation is however much smaller than around the $[\bar{1}2\bar{1}]_c$ axis and the generated mechanical stress does not induce a deep restructuring of the lattices.

Apart from the lattice rotation a close inspection of the reciprocal space coordinates of the diffuse x-ray scattering tails around the Bragg peaks of a -domains show that the interreticular distances are also modified at the intersections. To quantify the induced structural changes we have measured 3D reciprocal space maps around different Bragg peaks. In figure 5(a) is shown a 3D map of GeTe thin film including the 222_c Bragg peak and also the non-symmetric $\bar{2}22_c$ Bragg peak (considering as reference for reciprocal space coordinates the c -domains). The $\bar{2}22_c$ Bragg peak is angularly distant by $\sim 71^\circ$ with respect to the normal to the surface. It probes the interreticular distance along the rhombohedron axis of one variant of a -domain. As for a -domains Bragg peaks around the 222_c , the Bragg peaks of the a -domains around $\bar{2}22_c$ Bragg re-

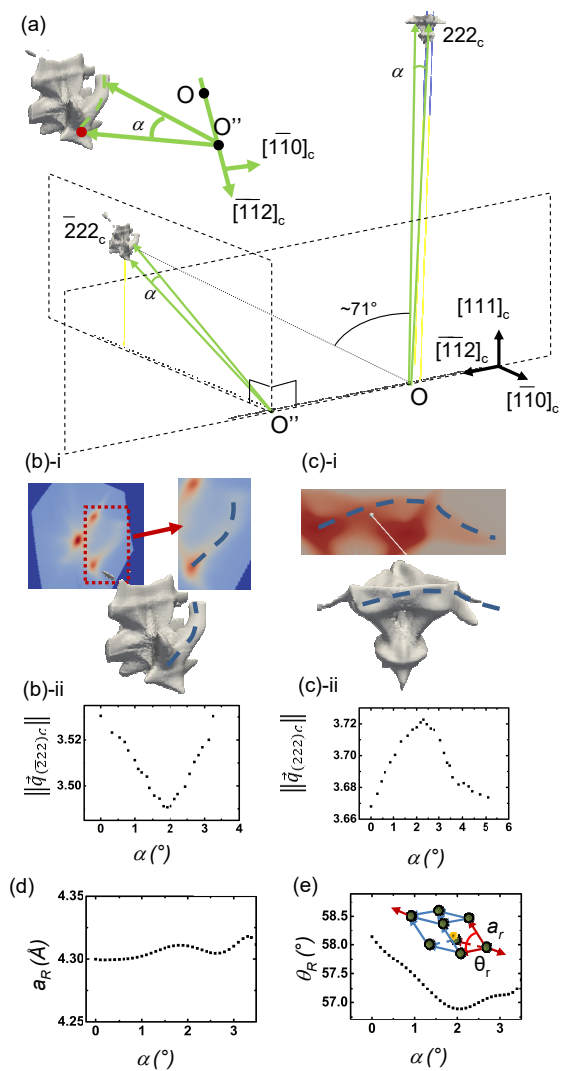


FIG. 5. (a) Complete 3D reciprocal space maps around $\bar{2}22_c$ and 222_c Bragg peaks (c -domains is selected as the reference domain for reciprocal space coordinates). (b)-(i) Close view of the 3D reciprocal space map around $\bar{2}22_c$. The dashed line illustrates the position of the diffuse tail starting from the a -domain Bragg peak. (b)-(ii) Evolution of the modulus of the scattering vector along the diffuse tail as function of the rotation angle α . (c) Same as (b) for the 222_c Bragg peak. (d) Plot of the rhombohedron lattice parameter at the intersection as function of rotation angle α . (e) Plot of the rhombohedron angle at the intersection as function of rotation angle α .

flexion shows diffuse scattering tails that can be assigned to lattice relaxations. In particular a diffuse tail starting from the Bragg peak of the a -domain that is stretched along the probed axis, i.e. the rhombohedron axis, extends far away [see figure 5(b)-(i)]. This tail can be assigned to a rotation of the lattice around $[\bar{1}12]_c$ direction as for the 222_c diffuse tail. In figures 5(b)-(ii) and (c)-(ii) are represented the evolution of the modulus of the scattering vectors as function of the lattice rotation angle

357 α following the diffuse scattering tails for 222_c and $\bar{2}22_c$
 358 Bragg peaks. For the 222_c diffuse tail, the modulus of the
 359 scattering vector increases from 36.6 nm^{-1} and reaches
 360 a maximum at 37.2 nm^{-1} (+1.6%) for $\alpha \sim 2^\circ$ and then
 361 decreases at larger angle. Similarly the modulus of the
 362 scattering vector of the $\bar{2}22_c$ diffuse tail decreases from
 363 35.3 to 34.9 nm^{-1} (-1.1%) for $\alpha \sim 2^\circ$ and then increases
 364 again at larger angle. The decrease of the modulus of
 365 the scattering vector of the $\bar{2}22_c$ diffuse tail clearly indi-
 366 cates an extension of the interlayer distance along the
 367 rhombohedron axis of the a -domain. This result is also
 368 corroborated by the decrease of the interlayer distance
 369 deduced from 222_c diffuse tail position. This set of data
 370 can be combined to determine the change of structure
 371 of the GeTe lattice in the intersection area. We could
 372 not detect a change of symmetry and the rhombohedral
 373 structure appears to be present even in the intersection
 374 area. Outside the intersections, from the Bragg peak
 375 positions, we obtain a rhombohedron lattice parameter
 376 $a_R = 0.430 \text{ nm}$ and angle $\theta_R = 58.2^\circ$. In the intersection
 377 area ($\alpha \sim 2^\circ$) we obtain a slight increase of the lattice
 378 parameter ($a_R = 0.431 - 0.432 \text{ nm}$) and a large decrease
 379 of the rhombohedron angle $\theta_R = 57.0^\circ$. Such a large
 380 structural modification is expected to result in a large
 381 change of ferroelectric polarization of the material.

382 Second-harmonic generation microscopy (SHG) with
 383 polarimetry analysis is used to examine and compare the
 384 local symmetry at the strip-domain (staircase) intersec-
 385 tions with respect to that of the parent material to de-
 386 tect a possible phase change at the intersections. The
 387 intersection regions are first detected using the K-means
 388 method applied to the SHG images recorded at differ-
 389 ent polarizer and analyzer angle settings, following the
 390 method reported in [27 and 30] and in the supplementary
 391 materials [22]. While the K-means clustering method al-
 392 lows the determination of the domain variants and infers
 393 the position of their intersections, it restricts the assign-
 394 ment of the data points to only one cluster. To disen-
 395 tangle the mixed signals from the main c -domain (back-
 396 ground) and the three different a -domains (nanostrips)
 397 in GeTe, especially at the a -domain intersections, we use
 398 the Non-Negative Matrix Factorization (NMF) algorithm
 399 on the SHG polarimetry data [27]. Because of the small
 400 size of the crossings (about 50 nm) and the long acquisi-
 401 tion time due to the slow sample scanning with respect to
 402 the laser in nonlinear optical microscopy, the SHG study
 403 contains a rather limited number of data points. To in-
 404 crease the accuracy of the data analysis, we trained the
 405 machine learning models on a larger data set, including
 406 the data reported in [24 and 27] (see supplementary ma-
 407 terials for details in [22]). Figure 6 summarizes the dif-
 408 ferent types of nanostrip crossings as automatically de-
 409 rived from the SHG polarimetry analysis using trained
 410 machine learning methods. Each SHG polarimetry plot
 411 associated with each pixel of the GeTe film can be decom-
 412 posed in four components with distinct polar plots corre-
 413 sponding to the contributions from the c -domain (black-
 414 background) and the 3 a -domains variants (RGB colors).

415 All detected crossing regions contain the signatures of the
 416 two a -domains forming the intersection. The intersection
 417 of strip domains can result in either uninterrupted or in-
 418 terrupted stripes, or a rearrangement of one of the inter-
 419 secting strip domains (e.g., splitting into two parts after
 420 crossing another a -domain). However, it is worth noting
 421 that the interrupted configuration (one of the strip do-
 422 mains is stopped at the intersection region) is most com-
 423 monly observed and occurs systematically in thin films
 424 with thicknesses below 400 nm . Decomposing the data
 425 into more than four polar plots does not provide relevant
 426 polar plots (see supplementary materials and figure 8 in
 427 [22]), showing that the intersections do not contain an
 428 additional phase. The absence of symmetry variation in
 429 the SHG study confirms that the a -domains at the inter-
 430 sections are rhombohedral.

431 The remaining question concerns the charge state of
 432 the $(\bar{1}01)_c$ 109° -type domain walls formed at these a/a
 433 domain intersections. Figure 7(a) is a schematic view of
 434 the polarization state of the c -domain and of two needle
 435 shape a -domains. Since the polarization state of the c -
 436 domain is along $[111]_c$, pointing upward [18], then to have
 437 a neutral 71° -type domain wall, the polarization state of
 438 the a -domains is expected to be along $[111]_c$ and $[\bar{1}\bar{1}\bar{1}]_c$.
 439 Therefore the formation of $(\bar{1}01)_c$ domain walls at a/a
 440 intersections results in non-compensated charges. The
 441 staircase morphology observed by STM [figure 7(b)] with
 442 alternate a -domains results in head-to-head and tail-to-
 443 tail polarization configurations at domain walls [figure
 444 7(c)]. The formation of charged domain walls in GeTe
 445 thin films seems to be driven by mechanical compati-
 446 bility, the electrostatic part being compensated by the
 447 available charges in the materials [31–33]. As proposed
 448 by Dangic and co-workers [7], charged domain walls are
 449 expected to be easily formed in GeTe. Indeed GeTe can
 450 provide free charge carriers to locally screen the accu-
 451 mulated charges since it is semiconducting and p-doped
 452 (due to the easy formation of Ge vacancies [34]). The
 453 positively charged carriers may compensate the accumu-
 454 lated charge at tail-to-tail domain walls whereas the cor-
 455 responding Ge vacancies (negatively charged) could accu-
 456 mulate at head-to-head domain walls if they are enough
 457 mobile [35]. Since screening by free charge carriers is
 458 expected to be much faster than by ions, the conductiv-
 459 ity at tail-to-tail domain walls should be higher than at
 460 head-to-head domain walls in GeTe.

IV. CONCLUSION

462 In conclusion we have studied the a -domain intersec-
 463 tions in ferroelectric GeTe thin films grown on Si(111)-Sb.
 464 Constrained by the mechanical compatibility conditions
 465 between a - and c -domains as well as by the epitaxy of the
 466 thin film with the silicon substrate, the a/a -domain in-
 467 tersections are *a priori* highly mismatched. To minimize
 468 the energy cost of these intersections, a complex struc-
 469 tural reorganization occurs as demonstrated by 3D re-

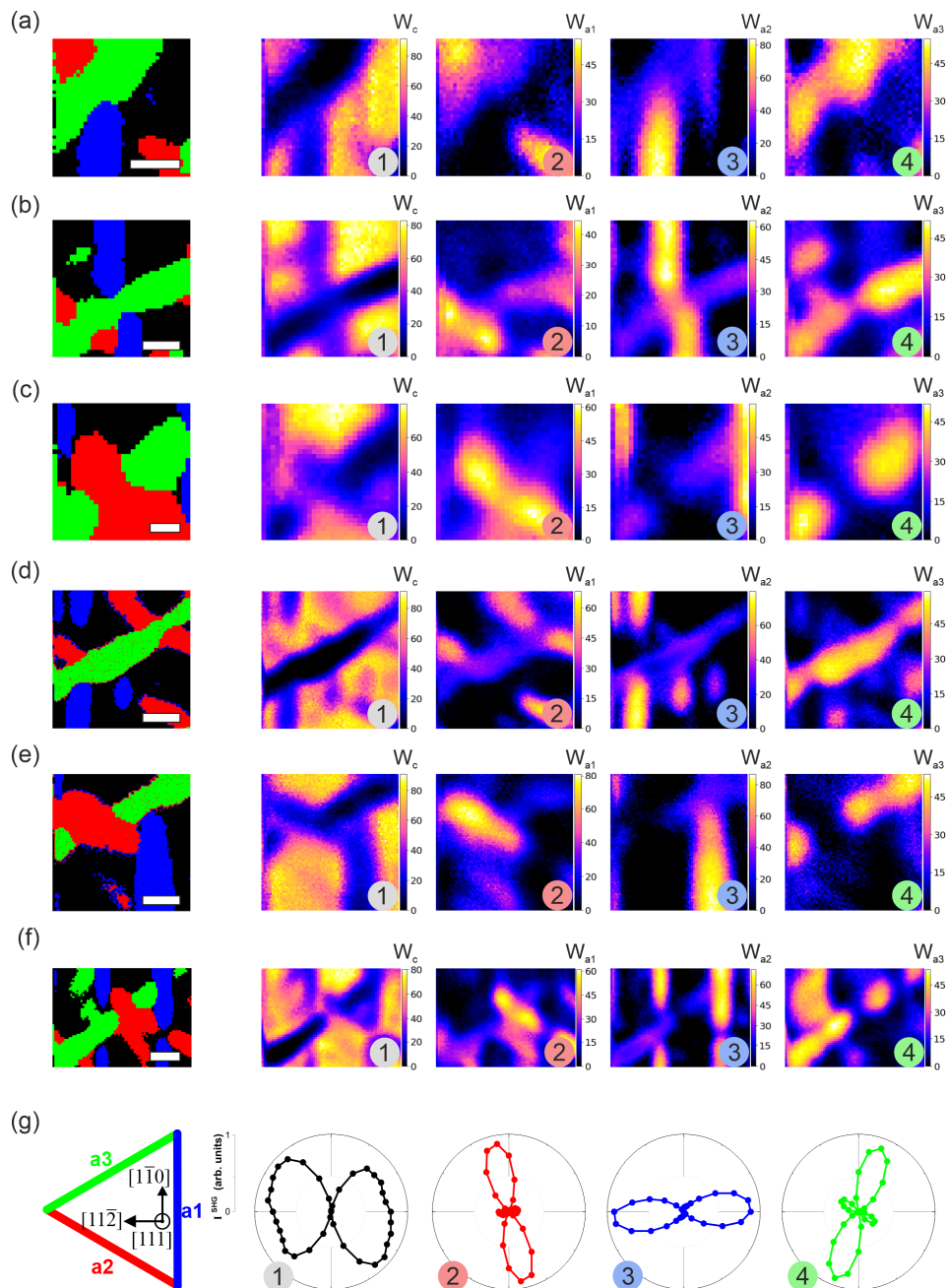


FIG. 6. Local (a)-(f) different strip domain intersection types derived from SHG microscopy polarimetry analysis assisted by trained K-means (left columns) and NMF algorithms at a -domains intersections. The domain contribution maps derived with NMF are obtained by taking into account four components (domain variants) with respective fractions W_i corresponding to the polar plots presented in panel (g). The scale bar is common to all images and corresponds to $1 \mu\text{m}$.

470 ciprocal space maps, scanning tunneling microscopy and 477 ization texture in GeTe thin films.
 471 second-harmonic generation. We demonstrate the for- 478 **Acknowledgements**
 472 mation of new domains walls, large lattice rotations, en- 479 The project leading to this publication has received
 473 hanced stretching of the rhombohedral lattice of GeTe. 480 funding from Excellence Initiative of Aix-Marseille Uni-
 474 We believe that the detailed description of a/a domain 481 versity A*MIDEX, a french "Investissements d'Avenir"
 475 intersections and 109° -type domain wall will motivate 482 programme through the AMUtech Institute. This work
 476 further studies for the control of the ferroelectric polar- 483 has also been supported by the ANR grant FETH (ANR-

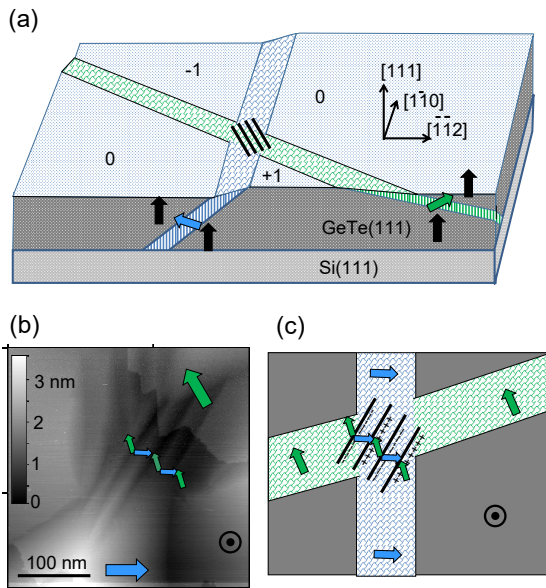


FIG. 7. (a) Model of the surface morphology and polarization states of *a*-domains and *c*-domain. (b) STM image of the surface topography of an intersecting area of two *a*-domains. The arrows show the in-plane components of the polarization direction at different places. (c) Corresponding schematic representation of the staircase morphology indicating the presence of charged domain walls.

484 22-CE08-0023). B. C. and S. C. -H. acknowledge the
 485 Interdisciplinary Thematic Institute EUR QMat (ANR-
 486 17-EURE-0024), as part of the ITI 2021-2028 program
 487 supported by the IdEx Unistra (ANR-10-IDEX-0002)
 488 and SFRI STRAT'US (ANR-20-SFRI-0012) through the
 489 French Programme d'Investissement d'Avenir. We deeply
 490 thank Lucio Martinelli for x-ray measurements (Syn-
 491 chrotron ESRF, BM32, Grenoble, France).

- 492 ¹ A. Gruverman, D. Wu, H-J Fan, I. Vrejoiu, M. Alexe, R. J. 521
 493 Harrison, and J. F. Scott, Vortex ferroelectric domains, 522
 494 Journal of Physics-Condensed Matter 20, 342201 (2008). 523
 495 ² N. Balke, B. Winchester, W. Ren, Y. H. Chu, A. N. 524
 496 Morozovska, E. A. Eliseev, M. Huijben, R. K. Vasude- 525
 497 van, P. Maksymovych, J. Britson, S. Jesse, I. Kornev, 526
 498 R. Ramesh, L. Bellaiche, L. Q. Chen, and S. V. Kalinin, 527
 499 Enhanced electric conductivity at ferroelectric vortex cores 528
 500 in BiFeO₃, Nature Physics 8, 81 (2012). 529
 501 ³ Y. L. Tang, Y. L. Zhu, X. L. Ma, A. Y. Borisevich, A. N. 530
 502 Morozovska, E. A. Eliseev, W. Y. Wang, Y. J. Wang, Y. B. 531
 503 Xu, Z. D. Zhang, and S. J. Pennycook, Observation of a 532
 504 periodic array of flux-closure quadrants in strained ferro- 533
 505 electric PbTiO₃ films, Science 348, 547 (2015). 534
 506 ⁴ A. K. Yadav, C. T. Nelson, S. L. Hsu, Z. Hong, J. D. 535
 507 Clarkson, C. M. Schlepueetz, A. R. Damodaran, P. Shafer, 536
 508 E. Arenholz, L. R. Dedon, D. Chen, A. Vishwanath, 537
 509 A. M. Minor, L. Q. Chen, J. F. Scott, L. W. Martin, and 538
 510 R. Ramesh, Observation of polar vortices in oxide super- 539
 511 lattices, Nature 530, 198 (2016). 540
 512 ⁵ P. Shafer, P. Garcia-Fernandez, P. Aguado-Puente, A. R. 541
 513 Damodaran, A. K. Yadav, C. T. Nelson, S.-L. Hsu, J. C. 542
 514 Wojdel, J. Iniguez, L. W. Martin, E. Arenholz, J. Jun- 543
 515 quera, and R. Ramesh, Emergent chirality in the electric 544
 516 polarization texture of titanate superlattices, Proceedings 545
 517 of the National Academy of Science USA 115, 915 (2018). 546
 518 ⁶ S. Das, Y. L. Tang, Z. Hong, M. A. P. Goncalves, M. R. 547
 519 McCarter, C. Klewe, K. X. Nguyen, F. Gomez-Ortiz, 548
 520 P. Shafer, E. Arenholz, V. A. Stoica, S. L. Hsu, B. Wang, 549
 C. Ophus, J. F. Liu, C. T. Nelson, S. Saremi, B. Prasad,
 A. B. Mei, D. G. Schlom, J. Iniguez, P. Garcia-Fernandez,
 D. A. Muller, L. Q. Chen, J. Junquera, L. W. Martin,
 and R. Ramesh, Observation of room-temperature polar
 skyrmions. Nature 568, 368 (2019).
⁷ D. Dangic, E. D. Murray, S. Fahy, and I. Savic, Structural
 and thermal transport properties of ferroelectric domain
 walls in GeTe from first principles. Physical Review B
 101, 184110 (2020).
⁸ D. Dangic, S. Fahy, and I. Savic, Giant thermoelectric
 power factor in charged ferroelectric domain walls of GeTe
 with Van Hove singularities. npj Computational Materials
 6, 195 (2020).
⁹ Min Hong, Jin Zou, and Zhi-Gang Chen. Thermoelec-
 tric GeTe with diverse degrees of freedom having secured
 superhigh performance. Advanced Materials 31, 1807071
 (2019).
¹⁰ Subhajit Roychowdhury, Manisha Samanta, Suresh Peru-
 mal, and Kanishka Biswas, Germanium chalcogenide ther-
 moelectrics: Electronic structure modulation and low lat-
 tice thermal conductivity, Chemistry of Materials 30, 5799
 (2018).
¹¹ Suresh Perumal, Subhajit Roychowdhury, and Kanishka
 Biswas, High performance thermoelectric materials and
 devices based on GeTe, Journal of Materials Chemistry C
 4, 7520 (2016).
¹² Juan Li, Xinyue Zhang, Siqi Lin, Zhiwei Chen, and
 Yanzhong Pei, Realizing the high thermoelectric perfor-
 mance of GeTe by Sb-doping and Se-alloying, Chemistry

- of Materials 29, 605 (2017).
- ¹³ E. M. Levin, M. F. Besser, and R. Hanus, Electronic and thermal transport in GeTe: A versatile base for thermoelectric materials, *Journal of Applied Physics* 114, 083713 (2013).
- ¹⁴ Wei-Di Liu, De-Zhuang Wang, Qingfeng Liu, Wei Zhou, Zongping Shao, and Zhi-Gang Chen, High-performance GeTe-based thermoelectrics: from materials to devices, *Advanced Energy Materials* 10, 2000367 (2020).
- ¹⁵ Xinyue Zhang, Zhonglin Bu, Siqi Lin, Zhiwei Chen, Wen Li, and Yanzhong Pei, GeTe thermoelectrics, *Joule* 4, 986 (2020).
- ¹⁶ D. Di Sante, P. Barone, R. Bertacco, and S. Picozzi, Electric Control of the Giant Rashba Effect in Bulk GeTe, *Advanced Materials* 25, 509 (2013).
- ¹⁷ A. V. Kolobov, D. J. Kim, A. Giussani, P. Fons, J. Tomimaga, R. Calarco, and A. Gruverman, Ferroelectric switching in epitaxial GeTe films, *APL Materials* 2, 066101 (2014).
- ¹⁸ C. Rinaldi, S. Varotto, M. Asa, J. Slawinska, J. Fujii, G. Vinai, S. Cecchi, D. Di Sante, R. Calarco, I. Vobornik, G. Panaccione, S. Picozzi, and R. Bertacco, Ferroelectric Control of the Spin Texture in GeTe, *Nano Letters* 18, 2751 (2018).
- ¹⁹ J. Krempasky, S. Muff, J. Minar, N. Pilet, M. Fanciulli, A. P. Weber, E. B. Guedes, M. Caputo, E. Mueller, V. V. Volobuev, M. Gmitra, C. A. F. Vaz, V Scagnoli, G. Springholz, and J. H. Dil, Operando Imaging of All-Electric Spin Texture Manipulation in Ferroelectric and Multiferroic Rashba Semiconductors, *Physical Review X* 8, 021067 (2018).
- ²⁰ Y. Li, Y. Li, P. Li, B. Fang, X. Yang, Y. Wen, D.-X. Zheng, C.-H. Zhang, X. He, A. Manchon, Z.-H. Cheng, and X.-X. Zhang, Nonreciprocal charge transport up to room temperature in bulk Rashba semiconductor alpha-GeTe. *Nature Communications* 12, 540 (2021).
- ²¹ Sara Varotto, Luca Nessi, Stefano Cecchi, Jagoda Slawinska, Paul Noel, Simone Petro, Federico Fagiani, Alessandro Novati, Matteo Cantoni, Daniela Petti, Edoardo Albisetti, Marcio Costa, Raffaella Calarco, Marco Buon giorno Nardelli, Manuel Bibes, Silvia Picozzi, Jean-Philippe Attane, Laurent Vila, Riccardo Bertacco, and Christian Rinaldi, Room-temperature ferroelectric switching of spin-to-charge conversion in germanium telluride, *Nature electronics* 4, 740 (2021).
- ²² See supplemental material at [publisher]. Relationship between the rhombohedral and the pseudo-cubic unit cells. Detailed methodology for the determination of ferroelectric domains structure measured by SHG.
- ²³ R. Wang, J. E. Boschker, E. Bruyer, D. Di Sante, S. Picozzi, K. Perumal, A. Giussani, H. Riechert, and R. Calarco, Toward Truly Single Crystalline GeTe Films: The Relevance of the Substrate Surface, *Journal of Physical Chemistry C* 118, 29724 (2014).
- ²⁴ B. Croes, F. Cheynis, Y. Zhang, C. Voulot, K. D. Dorkenoo, S. Cherifi-Hertel, C. Mocuta, M. Texier, T. Cornelius, O. Thomas, M.-I. Richard, P. Müller, S. Curiotto, and F. Leroy, Ferroelectric nanodomains in epitaxial GeTe thin films, *Physical Review Materials* 5, 124415 (2021).
- ²⁵ Karthick Perumal, *Epitaxial growth of Ge-Sb-Te based phase change materials*. PhD thesis, Humboldt-Universität zu Berlin, Mathematisch-Naturwissenschaftliche Fakultät I, (2013).
- ²⁶ S. Cherifi-Hertel, C. Voulot, U. Acevedo-Salas, Y. Zhang, O. Grégut, K. D. Dorkenoo, R. Hertel, Shedding light on non-Ising polar domain walls: Insight from second harmonic generation microscopy and polarimetry analysis, *Journal of Applied Physics* 2, 2200037 (2022).
- ²⁷ B. Croes, I. Gaponenko, C. Voulot, O. Grégut, K. D. Dorkenoo, F. Cheynis, S. Curiotto, P. Müller, F. Leroy, K. Cordero-Edwards, P. Paruch, S. Cherifi-Hertel, Automatic Ferroelectric Domain Pattern Recognition Based on the Analysis of Localized Nonlinear Optical Responses Assisted by Machine Learning, *Advanced Physics Research* 2, 2200037 (2022).
- ²⁸ F. Pedregosa, G. Varoquaux, A. Gramfort, V. Michel, B. Thirion, O. Grisel, M. Blondel, P. Prettenhofer, R. Weiss, V. Dubourg, J. Vanderplas, A. Passos, D. Cournapeau, M. Brucher, M. Perrot, E. Duchesnay, Scikit-learn: Machine Learning in Python, *Journal of Machine Learning Research* 12, 2825 (2011)
- ²⁹ B. Croes, F. Cheynis, P. Müller, S. Curiotto, and F. Leroy, Polar surface of ferroelectric nanodomains in GeTe thin films, *Physical Review Materials* 6, 064407 (2022).
- ³⁰ I. Gaponenko, S. Cherifi-Hertel, U. Acevedo-Salas, N. Bassiri-Gharb, and P. Paruch, Correlative imaging of ferroelectric domain walls, *Scientific Reports* 12, 165 (2022).
- ³¹ Arnaud Crassous, Tomas Sluka, Alexander K. Tagantsev, and Nava Setter, Polarization charge as a reconfigurable quasi-dopant in ferroelectric thin films, *Nature Nanotechnology* 10, 614 (2015).
- ³² Tomas Sluka, Petr Bednyakov, Alexander K. Tagantsev, and Nava Setter, Free-electron gas at charged domain walls in insulating BaTiO₃, *Nature Communications* 4, 1808 (2013).
- ³³ Petr S. Bednyakov, Tomas Sluka, Alexander K. Tagantsev, Dragan Damjanovic, and Nava Setter, Formation of charged ferroelectric domain walls with controlled periodicity, *Scientific Reports* 5, 15819 (2015).
- ³⁴ V. L. Deringer, M. Lumeij, and R. Dronskowski, Ab Initio Modeling of alpha-GeTe(111) Surfaces, *Journal of Physical Chemistry C* 116, 15801 (2012).
- ³⁵ Volker L. Deringer, Marck Lumeij, Ralf P. Stoffel, and Richard Dronskowski, Mechanisms of atomic motion through crystalline GeTe, *Chemistry of Materials* 25, 2220 (2013).